Research Article

Nano Research
2020, 13(11): 3048–3056

ISSN 1998-0124 CN 11-5974/O4
https://doi.org/10.1007/s12274-020-2970-y

Vertically aligned reduced graphene oxide/$Ti_3C_2T_x$ MXene hybrid hydrogel for highly efficient solar steam generation

Wei Li[1], Xiaofeng Li[1] (✉), Wei Chang[1], Jing Wu[1], Pengfei Liu[1], Jianjun Wang[2], Xi Yao[3], and Zhong-Zhen Yu[1,4] (✉)

[1] *State Key Laboratory of Organic–Inorganic Composites, College of Materials Science and Engineering, Beijing University of Chemical Technology, Beijing 100029, China*
[2] *Institute of Chemistry, Chinese Academy of Sciences, Beijing 100190, China*
[3] *Department of Biomedical Sciences, City University of Hong Kong, Hong Kong 999077, China*
[4] *Beijing Key Laboratory of Advanced Functional Polymer Composites, Beijing University of Chemical Technology, Beijing 100029, China*

Received: 22 March 2020 / **Revised:** 29 May 2020 / **Accepted:** 3 July 2020

ABSTRACT

Effective utilization of abundant solar energy for desalination of seawater and purification of wastewater is one of sustainable techniques for production of clean water, helping relieve global water resource shortage. Herein, we fabricate a vertically aligned reduced graphene oxide/$Ti_3C_2T_x$ MXene (A-RGO/MX) hybrid hydrogel with aligned channels as an independent solar steam generation device for highly efficient solar steam generation. The vertically aligned channels, generated by a liquid nitrogen-assisted directional-freezing process, not only rapidly transport water upward to the evaporation surface for efficient solar steam generation, but also facilitate multiple reflections of solar light inside the channels for efficient solar light absorption. The deliberate slight reduction endows the RGO with plenty of polar groups, decreasing the water vaporization enthalpy effectively and hence accelerating water evaporation efficiently. The MXene sheets, infiltrated inside the A-RGO hydrogel on the basis of Marangoni effect, enhance light absorption capacity and photothermal conversion performance. As a result, the A-RGO/MX hybrid hydrogel achieves a water evaporation rate of 2.09 $kg \cdot m^{-2} \cdot h^{-1}$ with a high conversion efficiency of 93.5% under 1-sun irradiation. Additionally, this photothermal conversion hydrogel rapidly desalinates seawater and purifies wastewater to generate clean water with outstanding ion rejection rates of above 99% for most ions.

KEYWORDS

anisotropic hydrogel, MXene, reduced graphene oxide, solar steam generation, aligned channels

1 Introduction

With the rapid development of industry and the increase of ever-growing population, the shortage of clean water is becoming a global crisis. Currently, most water purification plants adopt low-temperature multi-effect distillation or reverse osmosis technology, which rely on high energy consumption and large centralized infrastructure, limiting their practical applications in offshore areas, small villages, or remote areas far from the grid. It is thus imperative to utilize sustainable and pollution-free new energy for water purification. So far, various new and unexhausted energy sources, including wind energy [1], solar energy [2–5], tidal energy [6], and geothermal energy [7], have been developed and utilized. Solar-driven steam generation for seawater desalination [8] and wastewater treatment [9] has attracted more and more attention in recent years. Low-grade solar energy can be transformed to high-grade thermal and steam energy by using photothermal conversion materials and composites [10]. The water evaporation rate depends mainly on the absorptivity of photothermal conversion materials as the solar steam generators. At present, there are mainly four types of optical absorption materials [11]: plasmonic nanoparticles [12–14], carbon-based materials [15, 16], near-infrared materials [17], and organic photothermal conversion materials including polypyrrole and polyaniline [18, 19]. Based on the concept of interfacial heating, the criteria for designing an efficient solar-driven water evaporation system include: (1) strong light absorption capability and excellent photothermal conversion efficiency; (2) efficient water uptake, abundant porous channels for water transport, and automatic and uninterrupted operation; and (3) low thermal conductivity for localizing the heat at the water-air interface.

On the basis of the above criteria, three-dimensional (3D) graphene aerogels and foams are promising photothermal materials due to their high specific surface area [15], outstanding light absorption [20], tunable pore architectures [21], and stability in high and low temperatures [22, 23]. In addition to graphene, the two-dimensional (2D) early transition metal carbides and nitrides (MXenes) sheets also exhibit attractive and tunable properties, such as high electrical conductivity, favorable hydrophilicity, and excellent mechanical properties. MXenes are a new family of multifunctional 2D materials with the chemical formula of $M_{n+1}X_nT_x$ [24], where M represents an early transition metal, X refers to carbon or nitrogen, T_x stands for the surface functional groups (e.g., OH, O, and F groups), and n = 1, 2 or 3 [25]. MXene sheets have shown fantastic performances in electromagnetic interference shielding [26] because of superior electrical conductivity [27]. In addition,

Address correspondence to Xiaofeng Li, xfli@mail.buct.edu.cn; Zhong-Zhen Yu, yuzz@mail.buct.edu.cn

both graphene or MXene membranes and 3D aerogels have been used for solar steam generation due to their excellent light absorption capacity and photothermal conversion efficiency [28–34]. The average water evaporation rate of 3D graphene networks reaches 1.62 $kg·m^{-2}·h^{-1}$ under 1-sun illumination, better than those of other carbon materials reported [35]. The newly developed 3D MXene network could reach 1.46 $kg·m^{-2}·h^{-1}$ under 1-sun illumination [36]. Due to the poor mechanical properties of pure MXene hydrogels, few reports have been reported in the field of photothermal. Actually, the solar-driven steam generation rates of these inorganic materials are relatively low as compared to hydrophilic polymer hydrogels. The hydrophilic groups in a polymer hydrogel network could reduce the water vaporization enthalpy and accelerate the water evaporation rate [37]. However, the polymer hydrogels usually suffer from shrinkage at high power irradiations. Therefore, much efforts have to be devoted to increasing the solar steam generation rate of inorganic materials or enhancing the structural stability of polymer hydrogels. At the same time, there are few reports about the influence of vaporization enthalpy of water in inorganic materials. If the structure and composition of inorganic materials can be controlled to effectively reduce the vaporization enthalpy of water, it will be an effective way to solve the problem of slow water evaporation rate.

Herein, we use a directional-freezing technique to fabricate vertically aligned reduced graphene oxide (A-RGO) hydrogels as efficient solar steam generation devices. Different from the conventional 3D graphene framework for solar steam generation [35], the graphene oxide (GO) precursor is slightly reduced intentionally, so that the resultant 3D RGO framework retains a large number of oxygen-containing functional groups, benefiting the decrease in water vaporization enthalpy. Additionally, the vertically aligned channels accelerate the upward transport of water to the evaporation surfaces. Considering that Ti_3C_2 has an outstanding internal light-to-heat conversion efficiency (i.e., 100%) [38], the hydrophilic $Ti_3C_2T_x$ MXene sheets are coated inside the A-RGO hydrogel framework on the basis of the Marangoni effect to generate vertically aligned RGO/MXene (A-RGO/MX) hybrid hydrogels. As a result, the optimal anisotropic hybrid hydrogel achieves an average water evaporation rate of 2.09 $kg·m^{-2}·h^{-1}$ with a high conversion efficiency of 93.5% under 1-sun illumination, higher than those of static non-folding inorganic materials reported previously. The influences of the A-RGO/MX hybrid hydrogels on the vaporization enthalpy and water evaporation rate are also analyzed in detail.

2 Results and discussion

Figure 1 schematically illustrates the preparation of RGO hydrogel and A-RGO/MX hybrid hydrogel. The Marangoni effect is a mass movement phenomenon caused by tension gradient between two liquid interfaces, which would help the infiltration of $Ti_3C_2T_x$ MXene sheets into the 3D network of RGO hydrogels. The RGO hydrogel, obtained by slightly reducing an aqueous dispersion of GO with ascorbic acid at 70 °C, is firstly immersed in ethanol to exchange water with ethanol, and then soaked in an aqueous suspension of MXene for infiltrating the MXene sheets into the hydrogel network on the basis of the Marangoni effect. The solvent exchange process is repeated several times to increase the MXene content in the RGO/MX hybrid hydrogel, in which the RGO and MXene sheets are distributed randomly. To facilitate the upward transport of water inside the hydrogel, a liquid nitrogen-assisted directional-freezing technology is used to vertically grow ice crystal pillars from the bottom of the RGO/MX hydrogel,

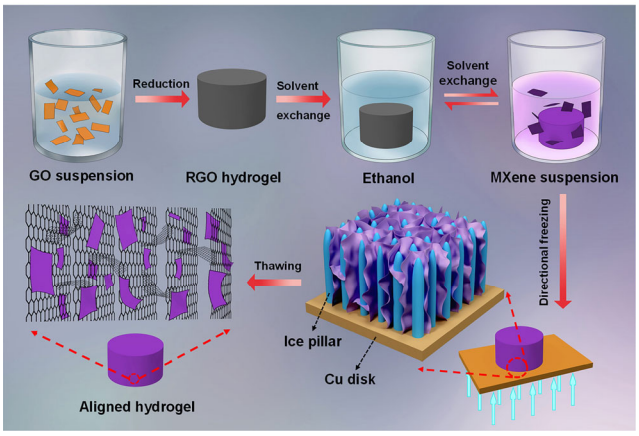

Figure 1 Schematic illustration of the fabrication of A-RGO/MX hybrid hydrogel.

during which the RGO and MXene sheets are expelled by the ice crystals and have to be vertically aligned among the pillars. After the ice melting, the resultant A-RGO/MX hybrid hydrogel exhibits numerous vertically aligned channels, benefiting the upward transport of water.

For comparison, the RGO/MX hydrogel and the A-RGO/MX hydrogel are freeze-dried to obtain porous aerogels by subliming the ice crystal pillars. Figures 2(a) and 2(b) show scanning electron microscope (SEM) images of the RGO/MX aerogel at different magnifications. As expected, a porous structure with numerous randomly distributed micron-scale pores is formed by self-assembly of the RGO sheets. Differently, the A-RGO/MX aerogel, obtained by freeze-drying the directionally frozen RGO/MX hydrogel to sublime its ice crystal pillars, exhibits many vertically aligned channels with diameters of 10–20 μm (Figs. 2(c)–2(e) and Fig. S1 in the Electronic Supplementary Material (ESM)). As shown in Fig. S2 in the ESM, the size of MXene sheets is in nanometer scale, which facilitates the MXene sheets to infiltrate into the RGO hydrogels with the micron-sized channels. The chemical compositions of the A-RGO/MX aerogel are characterized with its elemental mapping (Figs. 2(e)–2(h)). Apparently, the carbon and oxygen elements derive from both RGO and MXene sheets (Figs. 2(f) and 2(g)). The Ti elements could come from $Ti_3C_2T_x$ sheets only and exhibit a uniform distribution in the whole region (Fig. 2(h)), indicating that the MXene sheets are really entered into the RGO hydrogel for generating the A-RGO/MX hybrid hydrogel. Different from the carbon and oxygen elements, the Ti element does not present an obviously aligned distribution, which may be attributed to the low $Ti_3C_2T_x$ content.

To evaluate the composition evolutions of GO powder, MXene powder, freeze-dried RGO hydrogel, and freeze-dried RGO/MX hydrogel, their Fourier transform infrared (FT-IR) spectra, X-ray photoelectron spectroscopy (XPS) patterns, and Raman spectra are provided (Figs. 2(i)–2(l)). The FT-IR spectrum of GO shows peaks at 3,410 and 1,622 cm^{-1}, corresponding to –OH and –C=O, respectively [39, 40]. These peaks are still observed in the FT-IR spectrum of RGO, and the residual oxygen-containing groups of RGO benefit keeping the hydrophilicity of the RGO hydrogel. Since the $Ti_3C_2T_x$ MXene sheets also possess the same peak of –C=O at 1,622 cm^{-1}, these oxygen-containing groups can form hydrogen bonds between RGO and MXene sheets, making MXene and RGO successfully combined [41]. In the FT-IR spectrum of freeze-dried RGO/MX hydrogel, the peak of –C=O moves to 1,581 cm^{-1}, which results from the interaction between the MXene sheets and the RGO hydrogel. The Raman spectra of freeze-dried RGO hydrogel, MXene powder, and freeze-dried RGO/MX hydrogel are shown

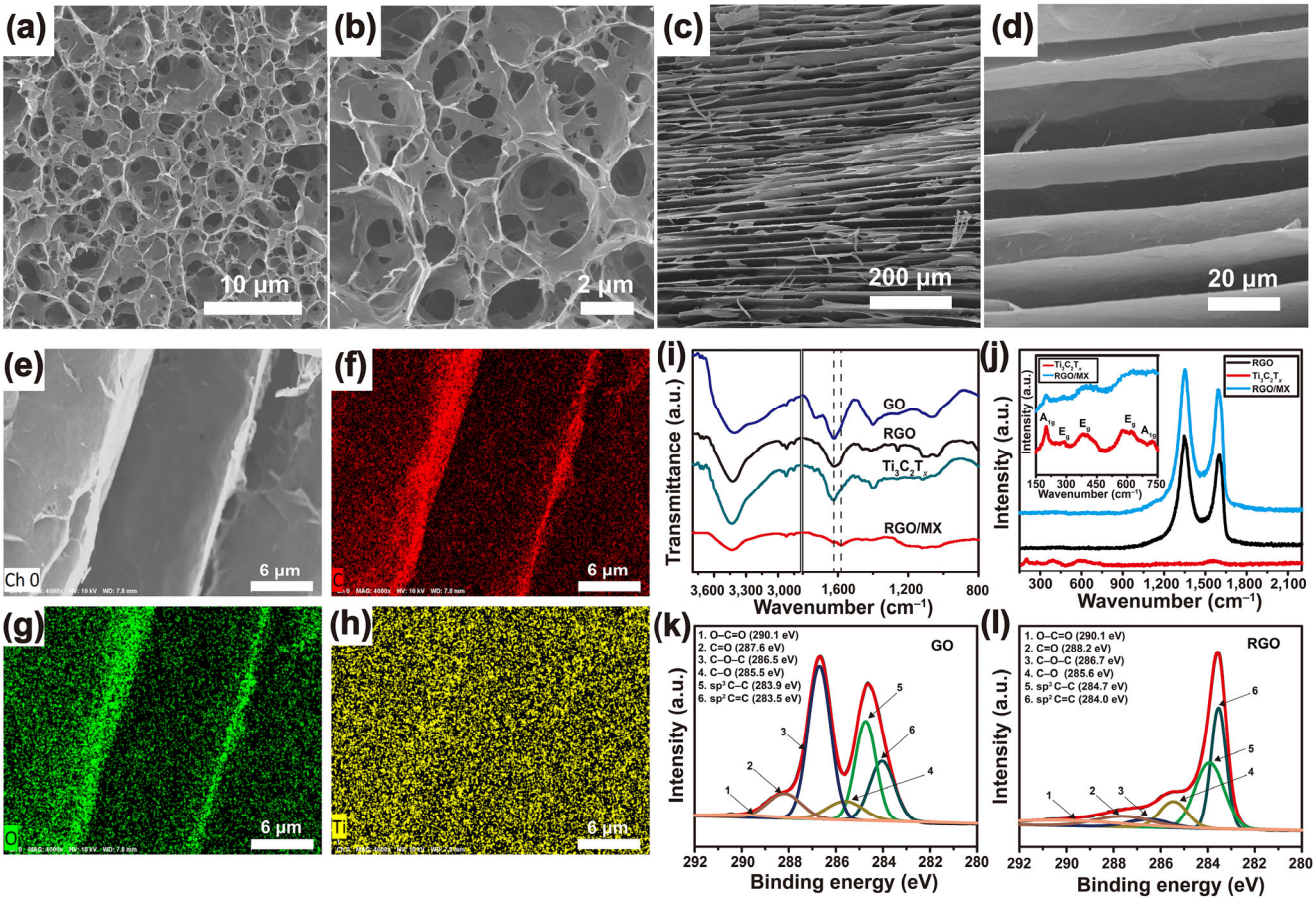

Figure 2 SEM images of freeze-dried RGO/MX hydrogel ((a) and (b)), freeze-dried A-RGO/MX hydrogel ((c)–(e)), and its mapping images of (f) C, (g) O, and (h) Ti elements. (i) FT-IR spectra of GO powder, $Ti_3C_2T_x$ MXene powder, freeze-dried RGO hydrogel, and freeze-dried RGO/MX hydrogel. (j) Raman spectra of MXene powder, freeze-dried RGO hydrogel, and freeze-dried RGO/MX hydrogel. C 1s XPS of (k) GO and (l) RGO.

in Fig. 2(j). Due to the relatively small content of MXene, the Raman spectrum of the RGO/MX is amplified in the range of 150–750 cm^{-1}, showing the peaks of both RGO and MXene. The observed peaks at 199 and 719 cm^{-1} correspond to the out of plane vibrations of Ti and C atoms. The modes at 287, 369, and 624 cm^{-1} are the E_g group vibrations including in-plane (shear) modes of Ti, C, and surface functional group atoms, verifying that the MXene sheets remain inside the RGO/MX hybrid hydrogel [25, 38, 42]. Moreover, there are two distinct peaks at 1,347 and 1,598 cm^{-1} in the Raman spectrum of RGO, corresponding to the D band associated with a breathing mode of the *K*-point phonons of the A_{1g} symmetry and the G band resulted from the first order scattering of the E_{2g} phonon of sp^2 C atoms [40, 43]. The X-ray diffraction (XRD) patterns of MXene powder, freeze-dried RGO hydrogel, and freeze-dried RGO/MX hydrogel are shown in Fig. S3 in the ESM. In the XRD pattern of MXene, a typical diffraction peak at ~ 7° is ascribed to $Ti_3C_2T_x$ [44]. The GO has a strong diffraction peak at ~ 11°, indicating its interlayer distance of 0.78 nm larger than that of pristine graphite (0.34 nm) because of the generated oxygen-containing groups. Differently, the RGO exhibits a broad peak at ~ 24°, illustrating the partial reduction of GO [45].

To investigate the structural evolutions of the GO architectures before and after the reduction, their XPS analyses are shown in Figs. 2(k) and 2(l) and Fig. S4 in the ESM. Because of the large number of oxygen-containing groups (e.g., carboxyl, epoxide, and hydroxyl) on the GO sheets, the C/O atomic ratio of GO is relatively low (~ 2.2). The RGO has an increased C/O atomic ratio (~ 4.8), which is still lower than those of many other RGO sheets obtained by chemical or thermal reductions [45–49], due to the slight reduction. The low C/O ratio indicates that the RGO sheets still have plenty residual oxygen-containing groups. The C 1s XPS of the RGO exhibits six peaks at 284.0, 284.7, 285.6, 286.7, 288.2, and 290.1 eV, corresponding to sp^2 C=C, sp^3 C–C, C–O, C–O–C, C=O, and O–C=O bonds, respectively [45]. The Ti 2p spectra of MXene and A-RGO/MX are shown in Fig. S5 in the ESM. Neat MXene shows several peaks at binding energies of 455.8, 458.2, 461.7 and 464.2 eV, corresponding to the bonds of Ti–C $2p_{3/2}$, Ti–O $2p_{3/2}$, Ti–C $2p_{1/2}$, and Ti–O $2p_{1/2}$, respectively. However, the Ti–O 2p spectrum of the A-RGO/MX shows a slight shift to higher binding energies, from 458.2 to 459.3 eV and from 464.2 to 465.1 eV. In addition, a new peak is observed at 456.8 eV, proving the formation of Ti–O–C covalent bonding between A-RGO and MXene [50]. The vertically aligned channel with hydrophilic surface makes the A-RGO/MX hybrid hydrogel promising for solar steam evaporation, and its evaporation tests are carried out using an on-line and real-time measurement system (Figs. S6(a) and S6(b) in the ESM).

Figure 3(a) shows a digital photo of the black A-RGO/MX hydrogel. Figure 3(b) presents the absorption spectra of RGO, A-RGO, RGO/MX, and A-RGO/MX hydrogels within ultraviolet (UV), visible, and near-infrared solar irradiation range (220–2,500 nm). Apparently, the A-RGO/MX hydrogel exhibits a high light absorption value of about 97%, and even 99% in the near-infrared range. Compared to the RGO hydrogel, the A-RGO hydrogel has a slight decrease in light absorption due to the aligned structure with large channels. With the presence of MXene sheets, the A-RGO/MX hydrogel displays an increased light absorption, which may be related to the multiple reflection

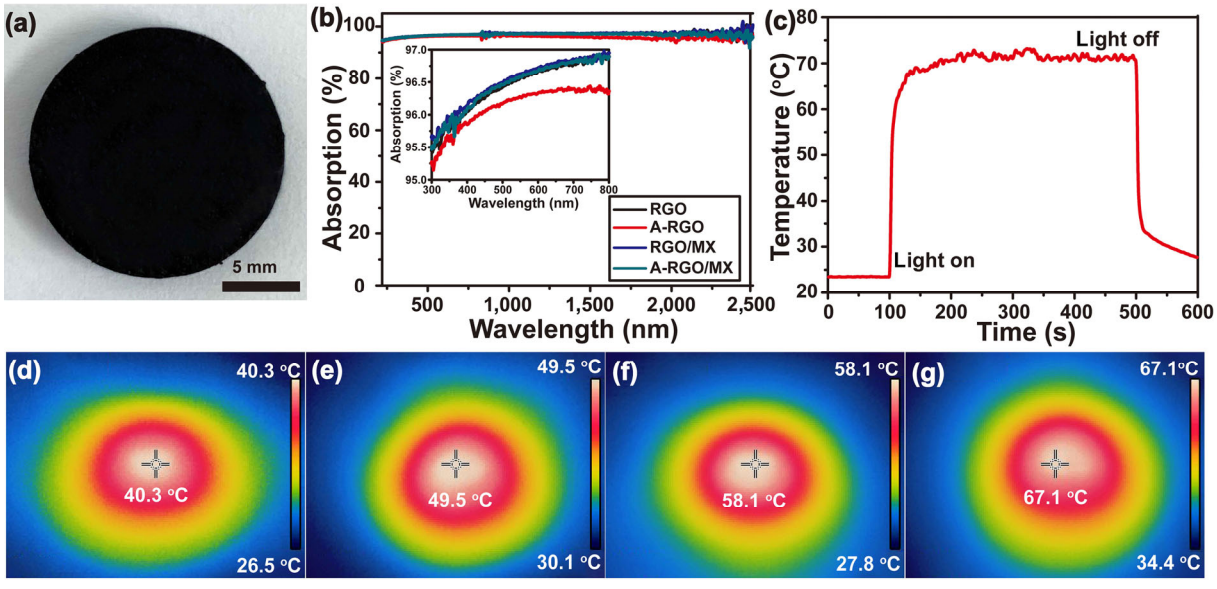

Figure 3 (a) Digital photo of A-RGO/MX hydrogel. (b) Absorbance spectra of RGO, A-RGO, RGO/MX, and A-RGO/MX hydrogels in the wavelength range of 220–2,500 nm (inset shows the absorbance spectra in the wavelength range of 220–800 nm). (c) Time trace of the temperature curve in response to light illumination for A-RGO/MX aerogel. Surface temperatures of A-RGO/MX hydrogel under (d) 1, (e) 3, (f) 5, and (g) 7 illumination intensities.

of light in the 3D network. Similarly, MXene and its composites also possess excellent electromagnetic interference shielding performances [26]. As a top-of-the-line electromagnetic interference shielding material, MXene almost does not allow electromagnetic waves to be emitted, and the absorbed electromagnetic waves eventually are dissipated in the form of heat inside the material [51]. It is reported that according to the Maxwell's equation, the higher conductivity, the greater the extinction coefficient, and thus the higher the electromagnetic wave absorption capacity [38]. The A-RGO/MX hydrogel is highly hydrophilic because of the presence of a large number of ions, and the oxygen-containing groups of both RGO and $Ti_3C_2T_x$ sheets. It takes only 0.3 s for absorbing water droplets and thus satisfying the prerequisite for water transport (Figs. S6(c) and S7 in the ESM). The hydrogels also show a great resistance to damage (Fig. S8 in the ESM).

Their surface temperatures are important for photothermal applications. Both the A-RGO/MX aerogel and hydrogel could effectively absorb light and convert the light to heat in a relatively short time (Fig. 3(c) and Fig. S9 in the ESM), facilitating the water steam generation. To minimize the heat exchange between the hydrogel and the substrate, the hydrogel is placed on a thermally insulating polystyrene foam and the steady-state temperatures of its surface are recorded by an infrared camera (Figs. 3(d)–3(g)). The surface temperatures of the A-RGO/MX hydrogel reach stable values of 40.3, 49.5, 58.1, and 67.1 °C under 1, 3, 5, and 7 sun irradiation intensities, respectively.

Figure 4(a) shows the variation curves of water mass changes without or with RGO, A-RGO, thermally treated RGO (T-RGO), RGO/MX, and A-RGO/MX hydrogels. The water mass changes are measured to be 1.82, 1.94, and 2.09 kg·m^{-2} for RGO, A-RGO, and A-RGO/MX hydrogels by 1-sun irradiation only for 1 h, respectively, much higher than that of pure water (0.33 kg·m^{-2}). It is noticed that the A-RGO hydrogel has a lower light absorption capacity than that of RGO hydrogel, but its vertically aligned channels benefit the upward water transport, leading to the increase in water evaporation rate. When the MXene sheets are infiltrated into the A-RGO hydrogel, the light absorption capacity of the hydrogel is enhanced (Fig. 3(b)). As a result, the water evaporation rate increases further. As far as we know, the water evaporation rate of the A-RGO/MX hybrid hydrogel is among the highest values of the static inorganic photothermal materials without a special folding structure, achieving a highest conversion efficiency of 93.5% at 1 kW·m^{-2} (Fig. 4(b) and Table S1 in the ESM) [20, 21, 35, 52–58]. Following the work of Zhao et al. [59], the equivalent enthalpy used in calculating the efficiency is not the same as that reported in the literature for inorganic photothermal materials (2,256 or 2,260 J·g^{-1}) [60, 61], but refers to the equivalent enthalpy (1,791 J·g^{-1}) estimated by our designed experiments in hydrogels, where the oxygen-containing functional groups have a significant effect on the vaporization enthalpy (Fig. S10 in the ESM). The water evaporation mechanism of the hydrogel is explained on the basis of Figs. 4(c)–4(e). Bound water is usually associated with water molecules that form hydrogen bonds with oxygen-containing functional groups on RGO skeleton or interact strongly with residual ions. Free water has a similar structure to bulk water, in which the interaction between water molecules and oxygen-containing functional groups on RGO skeleton can be neglected. Intermediate water is in a state between free water and bound water, and it has weak interactions with the oxygen-containing functional groups [62–64]. These three types of water molecules can be characterized by Raman spectra [62, 63]. It is reported that the evaporation rate of intermediate water is 86 times that of free water, so the higher content of intermediate water implies the faster evaporation of water [37].

Figure 4(d) shows the Raman spectra obtained by fitting the data using the Gaussian function of pure water to prove the existence of different types of water molecules, from which four peaks of water are observed at 3,233, 3,401, 3,514, and 3,630 cm^{-1} [59]. These peaks are classified as two types of modes: (1) water molecules with four hydrogen bonds, i.e., two protons and two lone electron pairs, are involved in the hydrogen bonding related to the peaks at 3,233 and 3,401 cm^{-1}; and (2) weakly or non-hydrogen-bonded water molecules, in which the hydrogen bonds of the water molecules are broken partly or entirely, correspond to the peaks at 3,514 and 3,630 cm^{-1} [37]. Within the bond corresponding to the four hydrogen-bonded molecules, the peak at 3,233 cm^{-1} is associated with the collective in-phase vibrations of all molecules in the aggregate, whereas the 3,401 cm^{-1} peak is associated with vibration, which

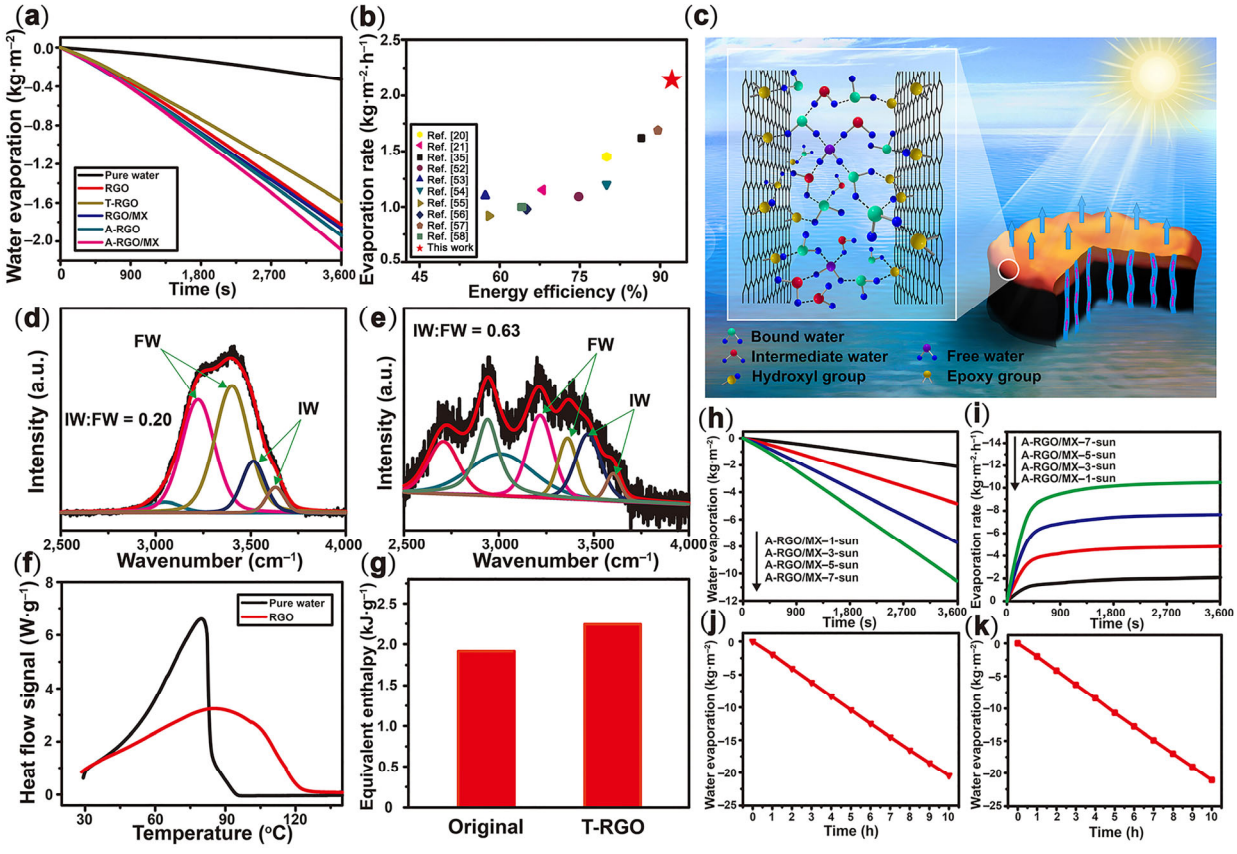

Figure 4 Solar steam generation performances of hydrogels. (a) Mass changes of water without or with RGO, T-RGO, A-RGO, and A-RGO/MX hydrogels under 1-sun irradiation. (b) Comparison of photothermal properties with those reported in the literature. (c) Diagrams of practical application of hydrogel and its water evaporation mechanism; fitting curves in the energy region of O–H stretching modes for water (d) without and (e) with the RGO hydrogel, where FW and IW represent free water and intermediate water, respectively. (f) Thermograms of pure water and RGO hydrogel. The magnitudes of DSC signals are proportional to the heat flow during the measurement. (g) Change of vaporization enthalpy of the RGO hydrogel before and after the thermal treatment at 200 °C. (h) Mass changes of water under each solar concentration. (i) Evaporation rates reach nearly the maximum value. Plot of mass change of (j) sea water and (k) pure water vs. time under 1-sun irradiation.

is not in-phase between the first and higher shell of neighboring molecules (i.e., the out-of-phase mode of O–H stretching). The peaks at 3,514 and 3,630 cm^{-1} correspond to the symmetric and asymmetric stretching of weakly hydrogen-bonded water molecules, respectively. The peak at 3,050 cm^{-1} arises from the Fermi resonance between the overtone of the bending mode [64].

Compared to pure water, the RGO hydrogel presents enhanced peaks of intermediate water. The molar ratio of intermediate water to free water in the RGO hydrogel is calculated to be 0.63, which is ~ 3.1 times that of pure water (Figs. 4(d) and 4(e)), contributing to the decrease in vaporization enthalpy for accelerating water evaporation. To prove the decrease in water vaporization enthalpy in the hydrogel, differential scanning calorimeter (DSC) is used to measure the evaporation energies of pure water and the water in the hydrogel (Fig. 4(f)). For pure water, after the heat flow signal reaches its maximum, it drops dramatically, indicating that the evaporation of water is completed immediately; whereas, the heat flow peak of the hydrogel becomes broader, and the heat flow signal decreases slowly with increasing the temperature, proving that the water evaporation in hydrogel is different from that of pure water. The DSC data in Table S2 in the ESM show that the water vaporization enthalpies in RGO, A-RGO, and A-RGO/MX hydrogels are much lower than that of pure water, which is because many water clusters in water are confined by the molecular meshes of graphene network and hence tend to evaporate easily as a result of the reduced overall energy consumption. The water molecules in liquid phase interact with each other by hydrogen bonds to form water clusters [65] with minimized energy by their configuration variations [66, 67]. In the absence of the hydrogels, water molecules are confined to the dynamically stabilized clusters and bounded by adjacent clusters [64], making the water evaporation relatively difficult. However, the water molecules in the RGO hydrogel could form hydrogen bonds with the oxygen-containing groups on the hydrogel network, thus some of those bounded clusters are activated. During the evaporation process, these water clusters would escape easily from the hydrogel network to the air, decreasing the water vaporization enthalpy and thus increasing the water evaporation rate [59]. Note that, because the DSC test is completely dehydrated while the evaporation is slightly dehydrated, the vaporization enthalpy measured by DSC could not be directly used to calculate the photothermal efficiency.

If the RGO hydrogel is freeze-dried and thermally reduced at 200 °C, the resultant T-RGO hydrogel has a higher water vaporization enthalpy than that of the RGO hydrogel (Fig. 4(g)). As a result, the water evaporation rate of T-RGO is only 1.58 $kg·m^{-2}·h^{-1}$ (Fig. 4(a)), which is a usual value for the graphene-based aerogel and carbon-based photothermal materials reported in the literature. The higher vaporization enthalpy of T-RGO may be ascribed to the decrease in its oxygen-containing groups that affect the state of water molecules. Apparently, the RGO hydrogel with a low reduction extent is beneficial for decreasing the vaporization enthalpy.

Figure S11 and Table S3 in the ESM show the effects of the

solvent exchange time on the water evaporation rate and the MXene content in RGO hydrogels. After two cycles of the solvent exchanges, the water evaporation rate of the A-RGO/MX hydrogel reaches a stable value. The hydrogels with the two-cycle solvent exchanges are used for the water evaporation performance evaluations unless otherwise specified. Figures 4(h) and 4(i) and Fig. S12 in the ESM show the influences of irradiation conditions on the water mass change and evaporation rate of the A-RGO/MX hydrogel. The evaporation rates of the A-RGO/MX hydrogel reach 2.09, 4.82, 7.66, and 10.48 $kg·m^{-2}·h^{-1}$ under 1, 3, 5, and 7 sun irradiations. Theoretically, the concentrated solar irradiation results in a higher input power density and the evaporation rate would increase with the solar energy. The increased ratio of water evaporation rate is approximately equal to the increased ratio of solar irradiation. However, in the present work, the actual evaporation rate value deviates from the theoretical value, which is attributed to the relatively low water transport rate in the hydrogel under concentrated solar irradiation. The A-RGO/MX hydrogel presents better structural stability and resistance to damage during shaking in water as compared to its counterpart obtained by directly mixing an aqueous suspension of GO and MXene followed by gelation (Fig. S13 in the ESM). Moreover, the A-RGO/MX hydrogel shows a stable performance even if it works continuously in sea water and pure water for 10 h (Figs. 4(j) and 4(k)).

Efficient use of the sustainable and pollution-free solar energy for water purifications is an effective means to solve the freshwater shortage. The A-RGO/MX hydrogel is used to purify the seawater obtained directly from Bohai Sea (Figs. 5(a) and 5(b)). The ion rejections of Na^+, Mg^{2+}, K^+, and Ca^{2+} in seawater are over 99%, and that of B^{3+} is also above 98%, demonstrating the excellent efficiency of the A-RGO/MX hydrogel in removing salt ions. The A-RGO/MX hydrogel provides the concentration changes of the four heavy metal ions in wastewater before and after the solar thermal purification (Figs. 5(c) and 5(d)). The rejections of Cr^{3+}, Pb^{2+}, Zn^{2+}, and Cu^{2+} ions are all above 99.9%. The water quality generated by solar thermal purification from seawater and wastewater fully conforms to the World Health Organization (WHO) standard for drinking water.

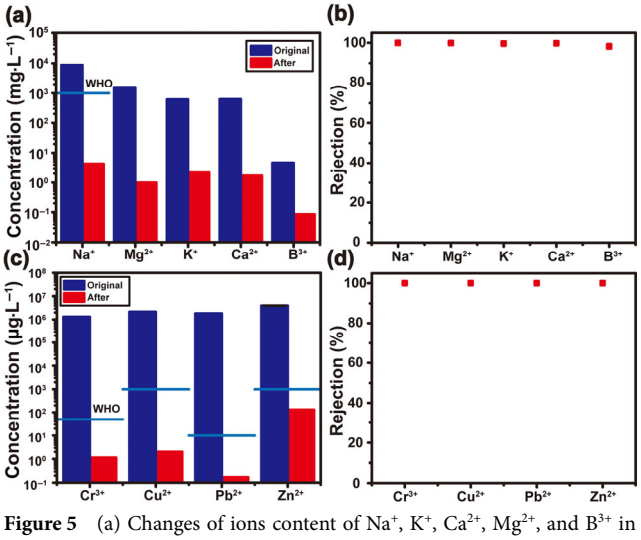

Figure 5 (a) Changes of ions content of Na^+, K^+, Ca^{2+}, Mg^{2+}, and B^{3+} in seawater before (original) and after solar thermal purification. (b) Ion rejection rate of seawater after solar thermal purification. (c) Changes of four primary ion concentrations of Cr^{3+}, Cu^{2+}, Zn^{2+}, and Pb^{2+} in simulated wastewater before (original) and after solar thermal purification (WHO standard at the short horizontal line). (d) Ion rejection rate of seawater after solar thermal purification.

3 Conclusions

A vertically aligned RGO/MX hybrid hydrogel is fabricated as an independent solar steam generation device for highly efficient solar steam generation. The vertically aligned channels are formed during the liquid nitrogen-assisted directional-freezing process, facilitating the upward transport of water to the evaporating surfaces for rapid generation of solar-driven steam. The partially reduced A-RGO/MX hydrogel possesses a large number of residual oxygen-containing groups and its anisotropic network not only enhances the multiple light absorption for heat generation, but also decreases the water vaporization enthalpy. As a result, the A-RGO/MX hydrogel achieves an outstanding water evaporation rate of 2.09 $kg·m^{-2}·h^{-1}$ with a high conversion efficiency of 93.5% under 1-sun illumination, better than those of static non-folding inorganic materials reported in the literature. Additionally, the A-RGO/MX hydrogel also presents prominent advantages in seawater desalination and wastewater purification with the rejection rates of more than 99% for most ions. These results indicate the great potential of the A-RGO/MX hydrogel for practical solar driven water treatment application.

4 Experimental

4.1 Materials

Pristine graphite flakes (300 mesh) were supplied by Huatai Lubricant and Sealing (China). $Ti_3C_2T_x$ aqueous solution was purchased from 11 Technology Co. Ltd (China). Sodium nitrate, sulfuric acid (98%), potassium permanganate (99.5%), hydrogen peroxide (30%), and hydrochloric acid (37%) were supplied by Beijing Chemical Factory (China). Ascorbic acid was provided by Aladdin Reagents (China). All chemicals and solvents were used as received without additional purification.

4.2 Preparation of RGO, A-RGO, T-RGO, and A-RGO/MX hydrogel

Graphite oxide was synthesized by oxidation of graphite flakes using a modified Hummers method [68], while the aqueous suspension of GO (4 $mg·mL^{-1}$) was obtained by ultrasonic exfoliation of the graphite oxide in deionized water for 15 min. After 5 mL of the GO suspension was heated at 75 °C for 1 h, 100 mg of ascorbic acid was added to chemically reduce the GO sheets, and the chemical reduction reaction lasts for 9 h at 70 °C to generate RGO hydrogels. Note that the bubble removal and preheating treatment were required before the reduction to avoid voids in the hydrogel. An A-RGO hydrogel was readily prepared by directional-freezing of the RGO hydrogel on a copper column pre-cooled by liquid nitrogen and subsequent thawing at an ambient environment. T-RGO hydrogel was obtained by heating the RGO aerogel at 200 °C for 2 h followed by absorbing water in a vacuum environment for 3 h. For the preparation of RGO/MX hydrogel, the RGO hydrogel was firstly immersed in ethanol to exchange water with ethanol, and then immersed in an aqueous suspension of $Ti_3C_2T_x$ MXene (4 $mg·mL^{-1}$). The Mxene sheets were incorporated into the hydrogel network with solvent exchange on the basis of the Marangoni effect. The RGO/MX hybrid hydrogel was placed on a copper column that was dipped in liquid nitrogen to form A-RGO/MX hybrid hydrogel with aligned channels by the directional-freezing treatment. To ensure the pass of water molecules, the dense layer of the upper and lower surfaces of the hydrogel were cut off. Before the test, the obtained hydrogels were immersed in deionized

water or seawater for 3 days to remove residual reactants and MXene.

4.3 Characterization

Morphologies and microstructures of all freeze-dried samples were observed with a JEOL JSM-7800F SEM. Energy dispersive X-ray (EDX) spectra were obtained using an energy-dispersive spectra detector. The samples were investigated using a Thermo VG RSCAKAB 250X high resolution XPS and a Renishaw InVia Raman microscopy with an excitation wavelength of 514 nm. X-ray diffraction data were recorded on a Rigaku D/Max 2500 XRD with Cu Kα radiation (0.154 nm) at a generator voltage of 40 kV and a generator current of 40 mA. Contact angles were characterized with a Data-Physics OCA 20 contact angle system at an ambient temperature. The vaporization enthalpy of water was measured by a TAQ2000 DSC at a heating rate of 5 °C·min^{-1}. A shimadzu UV-3600 ultraviolet-visible (UV-vis) spectrophotometer was used to measure diffuse reflection and transmission of hydrogels. Ion concentration of water was analyzed using an ICPS-7500 inductively coupled plasma emission spectrometer.

4.4 Steam generation and solar desalination

The A-RGO/MX hybrid hydrogel was put into a self-made glass mold containing proper amounts of water and exposed to solar irradiation for 60 min at steady-state condition with different solar irradiation intensities using a CEL-HXUV300 solar simulator with an optical filter for the standard AM 1.5 G spectrum. An OHAUS CP214 electronic balance with a resolution of 0.1 mg was used to record the mass change of water. Real-time data transmission was achieved by connecting a computer and the electronic balance with RS 232 serial ports. To investigate solar desalination capacity, the sea water obtained from the Bohai Sea (China) was directly used for salt removal. Waste water with heavy metal ions was prepared by dissolving certain amounts of copper nitrate, chromium chloride, lead nitrate, and zinc chloride in ultrapure water. The room temperature was 20 ± 2 °C and the ambient humidity was about 50%.

4.5 Estimation of water evaporation rates and energy conversion

Evaporation rate and photothermal conversion efficiency during the solar steam generation from solar energy to thermal energy are two important indicators for evaluating the performances. Equations (1) and (2) were used to calculate the evaporation rate and the conversion efficiency on the basis of the changes in water evaporation amounts [69]. The evaporation rate (v) can be calculated using the Eq. (1)

$$v = \frac{\mathrm{d}m}{S \times \mathrm{d}t} \quad (1)$$

where m is the mass of water evaporation, S is the surface area of a sample directly exposed to the simulated solar light, and t is exposure time. The solar thermal conversion efficiency (η) is defined in Eq. (2)

$$\eta = vh_{\mathrm{LV}}/(C_{\mathrm{opt}} \cdot P_0) \quad (2)$$

where h_{LV} is the equivalent enthalpy of the water in hydrogel, C_{opt} is the optical concentration, and P_0 refers to the nominal solar irradiation value of 1 kW·m^{-2}. When calculating the photothermal conversion efficiency, the evaporation rate of pure water under dark conditions ($v = v_{\mathrm{light}} - v_{\mathrm{dark}}$) should be deducted to eliminate the influence of natural water evaporation.

Acknowledgements

The authors acknowledge financial support from the National Natural Science Foundation of China (Nos. 51773008, 51533001, and U1905217) and the Fundamental Research Funds for the Central Universities (No. XK1802).

Electronic Supplementary Material: Supplementary material (SEM, transmission electron microscope (TEM), XRD pattern, XPS, contact angle, images, temperature curve, calculation of enthalpy of vaporization, thermal gravimetric analysis (TGA), water evaporation rates, stability performance, etc.) is available in the online version of this article at https://doi.org/10.1007/s12274-020-2970-y.

References

[1] Okumus, I.; Dinler, A. Current status of wind energy forecasting and a hybrid method for hourly predictions. *Energy Convers. Manag.* **2016**, *123*, 362–371.

[2] Liu, K. K.; Jiang, Q. S.; Tadepalli, S.; Raliya, R.; Biswas, P.; Naik, R. R.; Singamaneni, S. Wood-graphene oxide composite for highly efficient solar steam generation and desalination. *ACS Appl. Mater. Interfaces* **2017**, *9*, 7675–7681.

[3] Li, Y. J.; Gao, T. T.; Yang, Z.; Chen, C. J.; Kuang, Y. D.; Song, J. W.; Jia, C.; Hitz, E. M.; Yang, B.; Hu, L. B. Graphene oxide-based evaporator with one-dimensional water transport enabling high-efficiency solar desalination. *Nano Energy* **2017**, *41*, 201–209.

[4] Ghafurian, M. M.; Niazmand, H.; Ebrahimnia-Bajestan, E.; Taylor, R. A. Wood surface treatment techniques for enhanced solar steam generation. *Renew. Energy* **2020**, *146*, 2308–2315.

[5] Gong, F.; Li, H.; Wang, W. B.; Huang, J. G.; Xia, D. W.; Liao, J. X.; Wu, M. Q.; Papavassiliou, D. V. Scalable, eco-friendly and ultrafast solar steam generators based on one-step melamine-derived carbon sponges toward water purification. *Nano Energy* **2019**, *58*, 322–330.

[6] Hashemi, M. R.; Neill, S. P.; Robins, P. E.; Davies, A. G.; Lewis, M. J. Effect of waves on the tidal energy resource at a planned tidal stream array. *Renew. Energy* **2015**, *75*, 626–639.

[7] Liu, Y. M.; Yu, S. T.; Feng, R.; Bernard, A.; Liu, Y.; Zhang, Y.; Duan, H. Z.; Shang, W.; Tao, P.; Song, C. Y. et al. A bioinspired, reusable, paper-based system for high-performance large-scale evaporation. *Adv. Mater.* **2015**, *27*, 2768–2774.

[8] Xu, W. C.; Hu, X. Z.; Zhuang, S. D.; Wang, Y. X.; Li, X. Q.; Zhou, L.; Zhu, S. N.; Zhu, J. Flexible and salt resistant janus absorbers by electrospinning for stable and efficient solar desalination. *Adv. Energy Mater.* **2018**, *8*, 1702884.

[9] Lou, J. W.; Liu, Y.; Wang, Z. Y.; Zhao, D. W.; Song, C. Y.; Wu, J. B.; Dasgupta, N.; Zhang, W.; Zhang, D.; Tao, P. et al. Bioinspired multifunctional paper-based RGO composites for solar-driven clean water generation. *ACS Appl. Mater. Interfaces* **2016**, *8*, 14628–14636.

[10] He, J. X.; Zhao, G. H.; Mu, P.; Wei, H. J.; Su, Y. N.; Sun, H. X.; Zhu, Z. Q.; Liang, W. D.; Li, A. Scalable fabrication of monolithic porous foam based on cross-linked aromatic polymers for efficient solar steam generation. *Sol. Energy Mater. Sol. Cells* **2019**, *201*, 110111.

[11] Sun, Y.; Gao, J. P.; Liu, Y.; Kang, H. Y.; Xie, M. H.; Wu, F. M.; Qiu, H. X. Copper sulfide-macroporous polyacrylamide hydrogel for solar steam generation. *Chem. Eng. Sci.* **2019**, *207*, 516–526.

[12] Tian, L. M.; Luan, J. Y.; Liu, K. K.; Jiang, Q. S.; Tadepalli, S.; Gupta, M. K.; Naik, R. R. Singamaneni, S. Plasmonic biofoam: A versatile optically active material. *Nano Lett.* **2016**, *16*, 609–616.

[13] Zhou, L.; Tan, Y. L.; Wang, J. Y.; Xu, W. C.; Yuan, Y.; Cai, W. S.; Zhu, S. N.; Zhu, J. 3D self-assembly of aluminium nanoparticles for plasmon-enhanced solar desalination. *Nat. Photonics* **2016**, *10*, 393–398.

[14] Aydin, K.; Ferry, V. E.; Briggs, R. M.; Atwater, H. A. Broadband polarization-independent resonant light absorption using ultrathin plasmonic super absorbers. *Nat. Commun.* **2011**, *2*, 517.

[15] Ito, Y.; Tanabe, Y.; Han, J. H.; Fujita, T.; Tanigaki, K.; Chen, M. W. Multifunctional porous graphene for high-efficiency steam generation by heat localization. *Adv. Mater.* **2015**, *27*, 4302–4307.

[16] Liu, J.; Liu, Q. L.; Ma, D. L.; Yuan, Y.; Yao, J. H.; Zhang, W.; Su, H.

L.; Su, Y. S.; Gu, J. J.; Zhang, D. Simultaneously achieving thermal insulation and rapid water transport in sugarcane stems for efficient solar steam generation. *J. Mater. Chem. A* **2019**, *7*, 9034–9039.

[17] Jung, H. S.; Han, J. Y.; Lee, J. H.; Lee, J. H.; Choi, J. M.; Kweon, H. S.; Han, J. H.; Kim, J. H.; Byun, K. M.; Jung, J. H. et al. Enhanced NIR radiation-triggered hyperthermia by mitochondrial targeting. *J. Am. Chem. Soc.* **2015**, *137*, 3017–3023.

[18] Wang, W. L.; Niu, J. F.; Guo, J. Y.; Yin, L. F.; Huang, H. M. *In situ* synthesis of PPy-Fe_xO_y-CTS nanostructured gel membrane for highly efficient solar steam generation. *Sol. Energy Mater. Sol. Cells* **2019**, *201*, 110046.

[19] Yin, X. Y.; Zhang, Y.; Guo, Q. Q.; Cai, X. B.; Xiao, J. F.; Ding, Z. F.; Yang, J. Macroporous double-network hydrogel for high-efficiency solar steam generation under 1 sun illumination. *ACS Appl. Mater. Interfaces* **2018**, *10*, 10998–11007.

[20] Li, X. Q.; Xu, W. C.; Tang, M. Y.; Zhou, L.; Zhu, B.; Zhu, S. N.; Zhu, J. Graphene oxide-based efficient and scalable solar desalination under one sun with a confined 2D water path. *Proc. Natl. Acad. Sci. USA* **2016**, *113*, 13953–13958.

[21] Zhu, M. W.; Li, Y. J.; Chen, F. J.; Zhu, X. Y.; Dai, J. Q.; Li, Y. F.; Yang, Z.; Yan, X. J.; Song, J. W.; Wang, Y. B. et al. Plasmonic wood for high-efficiency solar steam generation. *Adv. Energy Mater.* **2018**, *8*, 1701028.

[22] Xu, Z.; Liu, Y. J.; Zhao, X. L.; Peng, L.; Sun, H. Y.; Xu, Y.; Ren, X. B.; Jin, C. H.; Xu, P.; Wang, M. et al. Ultrastiff and strong graphene fibers via full-scale synergetic defect engineering. *Adv. Mater.* **2016**, *28*, 6449–6456.

[23] Huang, R. L.; Huang, M. L.; Li, X. F.; An, F.; Koratkar, N.; Yu, Z. Z. Porous graphene films with unprecedented elastomeric scaffold-like folding behavior for foldable energy storage devices. *Adv. Mater.* **2018**, *30*, 1707025.

[24] Naguib, M.; Kurtoglu, M.; Presser, V.; Lu, J.; Niu, J. J.; Heon, M.; Hultman, L.; Gogotsi, Y.; Barsoum, M. W. Two-dimensional nanocrystals produced by exfoliation of Ti_3AlC_2. *Adv. Mater.* **2011**, *23*, 4248–4253.

[25] Yue, Y.; Liu, N. S.; Ma, Y. N.; Wang, S. L.; Liu, W. J.; Luo, C.; Zhang, H.; Cheng, F.; Rao, J. Y.; Hu, X. K. et al. Highly self-healable 3D microsupercapacitor with MXene-graphene composite aerogel. *ACS Nano* **2018**, *12*, 4224–4232.

[26] Liu, J.; Zhang, H. B.; Sun, R. H.; Liu, Y. F.; Liu, Z. S.; Zhou, A. G.; Yu, Z. Z. Hydrophobic, flexible, and lightweight MXene foams for high-performance electromagnetic-interference shielding. *Adv. Mater.* **2017**, *29*, 1702367.

[27] Zhou, Z. H.; Liu, J. Z.; Zhang, X. X.; Tian, D.; Zhan, Z. Y.; Lu, C. H. Ultrathin MXene/calcium alginate aerogel film for high-performance electromagnetic interference shielding. *Adv. Mater. Interfaces* **2019**, *6*, 1802040.

[28] Zhao, J. Q.; Yang, Y. W.; Yang, C. H.; Tian, Y. P.; Han, Y.; Liu, J.; Yin, X. T.; Que, W. Q. A hydrophobic surface enabled salt-blocking 2D Ti_3C_2 MXene membrane for efficient and stable solar desalination. *J. Mater. Chem. A* **2018**, *6*, 16196–16204.

[29] Zhao, X.; Zha, X. J.; Pu, J. H.; Bai, L.; Bao, R. Y.; Liu, Z. Y.; Yang, M. B.; Yang, W. Macroporous three-dimensional MXene architectures for highly efficient solar steam generation. *J. Mater. Chem. A* **2019**, *7*, 10446–10455.

[30] Zha, X. J.; Zhao, X.; Pu, J. H.; Tang, L. S.; Ke, K.; Bao, R. Y.; Bai, L.; Liu, Z. Y.; Yang, M. B.; Yang, W. Flexible anti-biofouling MXene/cellulose fibrous membrane for sustainable solar-driven water purification. *ACS Appl. Mater. Interfaces* **2019**, *11*, 36589–36597.

[31] Zhao, X.; Zha, X. J.; Tang, L. S.; Pu, J. H.; Ke, K.; Bao, R. Y.; Liu, Z. Y.; Yang, M. B.; Yang, W. Self-assembled core-shell polydopamine@MXene with synergistic solar absorption capability for highly efficient solar-to-vapor generation. *Nano Res.* **2020**, *13*, 255–264.

[32] Zhang, P. P.; Liao, Q. H.; Yao, H. Z.; Cheng, H. H.; Huang, Y. X.; Yang, C.; Jiang, L.; Qu, L. T. Three-dimensional water evaporation on a macroporous vertically aligned graphene pillar array under one sun. *J. Mater. Chem. A* **2018**, *6*, 15303–15309.

[33] Zhao, X.; Peng, L. M.; Tang, C. Y.; Pu, J. H.; Zha, X. J.; Ke, K.; Bao, R. Y.; Yang, M. B.; Yang, W. All-weather-available, continuous steam generation based on the synergistic photo-thermal and electro-thermal conversion by MXene-based aerogels. *Mater. Horiz.* **2020**, *7*, 855–865.

[34] Ju, M. M.; Yang, Y. W.; Zhao, J. Q.; Yin, X. T.; Wu, Y. T.; Que, W. X. Macroporous 3D MXene architecture for solar-driven interfacial water evaporation. *J. Adv. Dielect.* **2019**, *9*, 1950047.

[35] Zhang, P. P.; Li, J.; Lv, L. X.; Zhao, Y.; Qu, L. T. Vertically aligned graphene sheets membrane for highly efficient solar thermal generation of clean water. *ACS Nano* **2017**, *11*, 5087–5093.

[36] Zhang, Q.; Yi, G.; Fu, Z.; Yu, H. T.; Chen, S.; Quan, X. Vertically aligned janus MXene-based aerogels for solar desalination with high efficiency and salt resistance. *ACS Nano* **2019**, *13*, 13196–13207.

[37] Zhou, X. Y.; Zhao, F.; Guo, Y. H.; Zhang, Y.; Yu, G. H. A hydrogel-based antifouling solar evaporator for highly efficient water desalination. *Energy Environ. Sci.* **2018**, *11*, 1985–1992.

[38] Li, R. Y.; Zhang, L. B.; Shi, L.; Wang, P. MXene Ti_3C_2: An effective 2D light-to-heat conversion material. *ACS Nano* **2017**, *11*, 3752–3759.

[39] Zhao, D.; Huang, J. C.; Zhong, Y.; Li, K.; Zhang, L. N.; Cai, J. High-strength and high-toughness double-cross-linked cellulose hydrogels: A new strategy using sequential chemical and physical cross-linking. *Adv. Funct. Mater.* **2016**, *26*, 6279–6287.

[40] Yang, J.; Li, X. F.; Han, S.; Zhang, Y. T.; Min, P.; Koratkar, N.; Yu, Z. Z. Air-dried, high-density graphene hybrid aerogels for phase change composites with exceptional thermal conductivity and shape stability. *J. Mater. Chem. A* **2016**, *4*, 18067–18074.

[41] Chen, Y.; Xie, X. Q.; Xin, X.; Tang, Z. R.; Xu, Y. J. $Ti_3C_2T_x$-based three-dimensional hydrogel by a graphene oxide-assisted self-convergence process for enhanced photoredox catalysis. *ACS Nano* **2019**, *13*, 295–304.

[42] Yan, J.; Ren, C. E.; Maleski, K.; Hatter, C. B.; Anasori, B.; Urbankowski, P.; Sarycheva, A.; Gogotsi, Y. Flexible MXene/graphene films for ultrafast supercapacitors with outstanding volumetric capacitance. *Adv. Funct. Mater.* **2017**, *27*, 1701264.

[43] Yang, J.; Li, X. F.; Han, S.; Yang, R. Z.; Min, P.; Yu, Z. Z. High-quality graphene aerogels for thermally conductive phase change composites with excellent shape stability. *J. Mater. Chem. A* **2018**, *6*, 5880–5886.

[44] VahidMohammadi, A.; Moncada, J.; Chen, H. Z.; Kayali, E.; Orangi, J.; Carrero, C. A.; Beidaghi, M. Thick and freestanding MXene/PANI pseudocapacitive electrodes with ultrahigh specific capacitance. *J. Mater. Chem. A* **2018**, *6*, 22123–22133.

[45] Shao, Y. L.; El-Kady, M. F.; Lin, C. W.; Zhu, G. Z.; Marsh, K. L.; Hwang, J. Y.; Zhang, Q. H.; Li, Y. G.; Wang, H. Z.; Kaner, R. B. 3D freeze-casting of cellular graphene films for ultrahigh-power-density supercapacitors. *Adv. Mater.* **2016**, *28*, 6719–6726.

[46] Qiu, L.; Liu, J. Z.; Chang, S. L. Y.; Wu, Y. Z.; Li, D. Biomimetic superelastic graphene-based cellular monoliths. *Nat. Commun.* **2012**, *3*, 1241.

[47] Xu, Y. X.; Sheng, K. X.; Li, C.; Shi, G. Q. Self-assembled graphene hydrogel via a one-step hydrothermal process. *ACS Nano* **2010**, *4*, 4324–4330.

[48] Tang, G. Q.; Jiang, Z. G.; Li, X. F.; Zhang, H. B.; Hong, S.; Yu, Z. Z. Electrically conductive rubbery epoxy/diamine-functionalized graphene nanocomposites with improved mechanical properties. *Compos. Part B: Eng.* **2014**, *67*, 564–570.

[49] Tang, G. Q.; Jiang, Z. G.; Li, X. F.; Zhang, H. B.; Dasari, A.; Yu, Z. Z. Three dimensional graphene aerogels and their electrically conductive composites. *Carbon* **2014**, *77*, 592–599.

[50] Zhou, T. Z.; Wu, C.; Wang, Y. L.; Tomsia, A. P.; Li, M. Z.; Saiz, E.; Fang, S. L.; Baughman, R. H.; Jiang, L.; Cheng, Q. F. Super-tough MXene-functionalized graphene sheets. *Nat. Commun.* **2020**, *11*, 2077.

[51] Shahzad, F.; Alhabeb, M.; Hatter, C. B.; Anasori, B.; Hong, S. M.; Koo, C. M.; Gogotsi, Y. Electromagnetic interference shielding with 2D transition metal carbides (MXenes). *Science* **2016**, *353*, 1137–1140.

[52] Shao, Y.; Jiang, Z. P.; Zhang, Y. J.; Wang, T. Z.; Zhao, P.; Zhang, Z.; Yuan, J. Y.; Wang, H. All-poly(ionic liquid) membrane-derived porous carbon membranes: Scalable synthesis and application for photothermal conversion in seawater desalination. *ACS Nano* **2018**, *12*, 11704–11710.

[53] Zhu, M. W.; Li, Y. J.; Chen, G.; Jiang, F.; Yang, Z.; Luo, X. G.; Wang, Y. B.; Lacey, S. D.; Dai, J. Q.; Wang, C. W. et al. Tree-inspired design for high-efficiency water extraction. *Adv. Mater.* **2017**, *29*, 1704107.

[54] Li, T.; Liu, H.; Zhao, X. P.; Chen, G.; Dai, J. Q.; Pastel, G.; Jia, C.; Chen, C. J.; Hitz, E.; Siddhartha, D. et al. Scalable and highly efficient mesoporous wood-based solar steam generation device: Localized heat, rapid water transport. *Adv. Funct. Mater.* **2018**, *28*, 1707134.

[55] Zhang, L. B.; Tang, B.; Wu, J. B.; Li, R. Y.; Wang, P. Hydrophobic light-to-heat conversion membranes with self-healing ability for interfacial solar heating. *Adv. Mater.* **2015**, *27*, 4889–4894.

[56] Chen, C. J.; Li, Y. J.; Song, J. W.; Yang, Z.; Kuang, Y. D.; Hitz, E.; Jia, C.; Gong, A.; Jiang, F.; Zhu, J. Y. et al. Highly flexible and efficient solar steam generation device. *Adv. Mater.* **2017**, *29*, 1701756.

[57] Cui, L. F.; Zhang, P. P.; Xiao, Y. K.; Liang, Y.; Liang, H. X.; Cheng, Z. H.; Qu, L. T. High rate production of clean water based on the combined photo-electro-thermal effect of graphene architecture. *Adv. Mater.* **2018**, *30*, 1706805.

[58] Zhou, L.; Tan, Y. L.; Ji, D. X.; Zhu, B.; Zhang, P.; Xu, J.; Gan, Q. Q.; Yu, Z. F.; Zhu, J. Self-assembly of highly efficient, broadband plasmonic absorbers for solar steam generation. *Sci. Adv.* **2016**, *2*, e1501227.

[59] Zhao, F.; Zhou, X. Y.; Shi, Y.; Qian, X.; Alexander, M.; Zhao, X. P.; Mendez, S.; Yang, R. G.; Qu, L. T.; Yu, G. H. Highly efficient solar vapour generation via hierarchically nanostructured gels. *Nat. Nanotechnol.* **2018**, *13*, 489–495.

[60] Wang, Y. C.; Wang, C. Z.; Song, X. J.; Megarajan, S. K.; Jiang, H. Q. A facile nanocomposite strategy to fabricate a rGO-MWCNT photothermal layer for efficient water evaporation. *J. Mater. Chem. A* **2018**, *6*, 963–971.

[61] Hua, Z. T.; Li, B.; Li, L. L.; Yin, X. Y.; Chen, K. Z.; Wang, W. Designing a novel photothermal material of hierarchical microstructured copper phosphate for solar evaporation enhancement. *J. Phys. Chem. C* **2017**, *121*, 60–69.

[62] Kitano, H.; Tada, S.; Mori, T.; Takaha, K.; Gemmei-Ide, M.; Tanaka, M.; Fukuda, M.; Yokoyama, Y. Correlation between the structure of water in the vicinity of carboxybetaine polymers and their blood-compatibility. *Langmuir* **2005**, *21*, 11932–11940.

[63] Terada, T.; Maeda, Y.; Kitano, H. Raman spectroscopic study on water in polymer gels. *J. Phys. Chem.* **1993**, *97*, 3619–3622.

[64] Sekine, Y.; Ikeda-Fukazawa, T. Structural changes of water in a hydrogel during dehydration. *J. Chem. Phys.* **2009**, *130*, 034501.

[65] Okumura, M.; Yeh, L. I.; Myers, J. D.; Lee, Y. T. Infrared spectra of the solvated hydronium ion: Vibrational predissociation spectroscopy of mass-selected $H_3O^+ \cdot (H_2O)_n \cdot (H_2)_m$. *J. Phys. Chem.* **1990**, *94*, 3416–3427.

[66] Miyazaki, M.; Fujii, A.; Ebata, T.; Mikami, N. Infrared spectroscopic evidence for protonated water clusters forming nanoscale cages. *Science* **2004**, *304*, 1134–1137.

[67] Jiang, J. C.; Wang, Y. S.; Chang, H. C.; Lin, S. H.; Lee, Y. T.; Niedner-Schatteburg, G.; Chang, H. C. Infrared spectra of $H^+(H_2O)_{5-8}$ clusters: Evidence for symmetric proton hydration. *J. Am. Chem. Soc.* **2000**, *122*, 1398–1410.

[68] An, F.; Li, X. F, ; Min, P.; Liu, P. F.; Jiang, Z. G.; Yu, Z. Z. Vertically aligned high-quality graphene foams for anisotropically conductive polymer composites with ultrahigh through-plane thermal conductivities. *ACS Appl. Mater. Interfaces* **2018**, *10*, 17383–17392.

[69] Ghasemi, H.; Ni, G.; Marconnet, A. M.; Loomis, J.; Yerci, S.; Miljkovic, N.; Chen, G. Solar steam generation by heat localization. *Nat. Commun.* **2014**, *5*, 4449.